CrossMark

A Search for Meteoroid Lunar Impact Generated Electromagnetic Pulses

Saiveena Kesaraju[1] · John D. Mathews[1] · Juha Vierinen[2] ·
Phil Perillat[3] · David D. Meisel[4]

Abstract Lunar white light flashes associated with meteoroid impacts are now regularly observed using modest optical instrumentation. In this paper, we hypothesize that the developing, optically-dense hot ejecta cloud associated with these hypervelocity impacts also produce an associated complex plasma component that rapidly evolves resulting in a highly-transient electro magnetic pulse (EMP) in the VHF/UHF spectral region. Discovery of the characteristics and event frequency of impact EMPs would prove interesting to meteoroid flux and complex plasma physics studies especially if EMPs from the same event are detected from at least two locations on the Earth with relative delays appropriate to the propagation paths. We describe a prototype observational search, conducted in May 2014, for meteoroid lunar-impact EMPs that was conducted using simultaneous, overlapping-band, UHF radio observations at the Arecibo (AO; Puerto Rico) and Haystack (HO, Massachusetts, USA) Observatories. Monostatic/bistatic lunar radar imaging observations were also performed with HO transmitting and HO/AO receiving to confirm tracking, the net delay, and the pointing/timing ephemeris at both observatories. Signal analysis was performed using time–frequency signal processing techniques. Although, we did not conclusively identify EMP returns, this search detected possible EMPs and we have confirmed the search paradigm and established the sensitivity of the AO–HO system in detecting the hypothesized events. We have also characterized the difficult radio-frequency interference environment surrounding these UHF observations. We discuss the wide range of terrestrial-origin, Moon-bounce signals that were observed which additionally validate the observational technique. Further observations are contemplated.

✉ John D. Mathews
JDMathews@psu.edu

1 Radar Space Sciences Lab, 323 Electrical Engineering East, The Pennsylvania State University, University Park, PA, USA

2 Haystack Observatory, Massachusetts Institute of Technology, Cambridge, MA, USA

3 Arecibo Observatory, Arecibo, PR, USA

4 Department of Physics and Astronomy, SUNY-Geneseo, Geneseo, NY, USA

Abbreviations

AO	Arecibo observatory
EMP	Electromagnetic pulse
FFT	Fast Fourier transform
HO	Haystack MISA antenna
ISAR	Inverse synthetic aperture radar
ITU	International Telecommunication Union
PRF	Pulse repetition frequency
RF	Radio frequency
STFT	Short time Fourier transform
TDRA	Time domain radio astronomy mode
TOMB	Terrestrial origin moon bounce
UHF	Ultra-high frequency
UT	Universal time

1 Introduction

In recent years, light flashes associated with hypervelocity meteoroid impacts on the Moon have been regularly observed using modest optical telescopes and modern camera systems. Observations from the NASA lunar impact monitoring program reported in Suggs et al. (2008, 2014) and of sporadic lunar impacts reported by Ortiz et al. (2006), Madiedo and Trigo-Rodriguez (2011), Madiedo et al. (2014), Larbi et al. (2015), Rembold and Ryan (2015) confirm that these impacts are readily visible from the Earth. The duration of these light flashes can be as long as ~ 1 s as recorded on March 17, 2013 and reported in Suggs et al. (2014). Most reports conclude that lunar impact light flash duration is likely mostly dependent on the net energy of the impact. That is, on the impact velocity (hypervelocity range: 10–70 km/s) and net mass and perhaps mass density and composition of the impact meteoroid. Note that the term "hypervelocity" is most correctly meant to indicate impactor speed greater than sound speed in the impacted material.

Additionally, theories developed by Close et al. (2010), Friichtenicht and Slattery (1963) indicate that plasma production is associated with the hypervelocity impacts in the initial stage of the impact process and that a meteoroid induced Electromagnetic pulse (EMP) is likely generated if sufficient net energy is available. We note that other sources of impact-related RF radiation may include electrostatic discharges from dust effects of the impact (Lee et al. 2012). In Foschini (1998), modeling calculations show that plasma produced during the impact of a meteoroid can produce electromagnetic radiation in the microwave frequency range for a typical Leonid meteoroid moving at a speed of 71 km/s, mass density of ~ 1 gm/cm^3, a radius of ~ 0.5 cm, and having a mass up to 8 gm. Nemtchinov et al. (1998) perform impact simulations by solving the two-dimensional radiative-gas dynamics problem based on the size and mass density of the impact material in order to estimate the time span of the RF radiation flux which is found to be of order 10^{-5}–10^{-3} s. Using the Colorado Center for Lunar Dust and Atmospheric Studies dust accelerator Collette et al. (2013) find the maximum ejecta temperature in the first 1 μs after impact compared with the longer duration (~ 20 μs) optical flash which corresponds to radiative cooling of the optically-dense ejecta "cloud". The plasma evolution phase, giving

rise to the EMP, apparently corresponds to the short-duration, high temperature early phase of the ejecta production and evolution.

Many laboratory experiments have been conducted to determine the RF emission characteristics from hypervelocity impacts induced plasma using different impact and target materials of diverse mass range. The objective of these experiments is to study the electrical anomalies caused in the satellites or spacecraft when in orbit due to meteoroid and space debris impacts. Close et al. (2013), Johnson et al. (2011) conducted experiments that detected the down-chirping (decreasing signal frequency with increasing time after impact) electromagnetic pulse (EMP) associated with the hypervelocity impact induced plasma evolution at impact speeds above 11 km/s as attained during meteor showers for microgram (mass $<10^{-6}$ g) iron particles. They used patch antennas operating at 315 and 916 MHz (UHF range) that have a bandwidth of 10 % of the center frequency along with a high frequency (>2 GHz) E-field sensor in detecting microsecond-duration EMP signals. Maki et al. (2004) also observed emissions at UHF and microwave frequencies using receivers at 500 MHz and 22 GHz and ~ 1 gm polycarbonate projectiles traveling at high speeds (~ 2, 4 and 6 km/s) impacting an aluminum target plate causing cratering and RF emission. The detected signals consisted of pulses having a net duration in the range of few tens of microseconds but were not associated with the primary impact optical signature. Further, Maki et al. (2005) studied the dependence of microwave emissions from hyper-velocity impacts particularly at 4 km/s on target materials including aluminum, alumina, ceramic, redbrick again using ~ 1 gm polycarbonate projectiles. The signals observed, in this case, had two waveforms: intermittent sharp pulses and signals with white noise/wideband characteristics. They conclude that for the applications on spacecraft, an impact detector in microwave region is more advantageous than the optical impact detection method.

Henceforth, based on the lunar optical flash observations, various theoretical hyper-velocity impact models, and laboratory experiments regarding RF emissions due to hypervelocity impacts discussed above, we hypothesize that when gram-sized, hyperve-locity meteoroids impact the Moon, RF electromagnetic pulses (EMPs) are generated in the initial stage of the impact ejecta evolution. Further, it is reasonable to assume from the above references that these EMPs will have duration of a few microseconds and a broad frequency extent that includes at least the V/UHF frequency region (30 MHz–3 GHz).

In the next sections, we describe our search paradigm towards unambiguously detecting these EMPs using the simultaneous 430–440 MHz region radio observations of the Moon from the Arecibo (AO) and Haystack (HO) Observatories. We make what seem to be relatively conservative assumptions in estimating the EMP detectability from these two observatories. In particular, we note that a 10^{-3} kg meteoroid striking the Moon at 20 km/s releases 2×10^5 J of kinetic energy. The net efficiency of plasma production and resultant RF emission is taken to be 0.01 % of the net kinetic energy on the basis that that the immediate temperature of the plasma is in the range of 20–40 eV (Ratcliff et al. 1997; Close et al. 2010) with initial plasma number density $\sim 10^{22}$ cm^{-3}. The estimate of total charge created in the initial impact volume is based on Eq. (1) of Close et al. (2010), which is discussed in more detail in McBride and McDonnell (1999). The net charge is taken to occupy the approximate volume of the meteoroid on impact thus yielding the estimate for initial electron number density. The plasma then evolves (expands with the ejecta, ambipolar electric fields established, etc.) over a few microseconds (Collette et al. 2013). The assumed net 20 J of the original 2×10^5 J of kinetic energy, when appearing as electromagnetic radiation in a 10 GHz bandwidth in 10^{-6} s, yields a power spectral density of ~ 0.002 Watts/Hz. Assuming the event radiates uniformly into half the sphere and

distance from Moon to the ground-based receiver as 384400 km over a 5 MHz bandwidth results in the power flux density of 10^{-14} watts/m^2 for the received signal. Further assuming 50 % antenna efficiency and antenna diameter of 305 m for AO gives the received power to be 3×10^{-10} Watts. For the noise power, we assume a receiver temperature of 50 K and a lunar UHF temperature of 200 K (Martinides 1965) over 5 MHz bandwidth that results in 1.7×10^{-14} Watts noise power. Thus the apparently conservative estimate of Signal-to-Noise (SNR) ratio for a 1 μs duration impact EMP is large—86 dB at AO and 54 dB at HO that has an antenna dish of the radius of 23 m. In addition to these favorable SNR calculations, these two systems were considered because of the overlap of their operating frequency range in the 430–440 MHz UHF radar band. Of course, approximately the same longitude is necessary to observing a common area on the lunar surface. Further, the relative path delay difference between a lunar EMP and AO/HO can be used to discriminate the lunar origin EMP signals against the impulsive local interference that is possible due to power-line arcing, etc. The relative delay is due to the differences in distance between the Moon and the two observatory locations and is approximately 2.5 ms (as determined by the ephemerides and as described in Sect. 2.1). Hence, a positive indication of a lunar-origin EMP is when an EMP-like signal is observed at both Haystack and Arecibo within an appropriate relative time delay window.

With an objective that these observations can be useful in studying the meteoroid-impact-ejecta complex plasma environment and its evolution during the process, the lunar-impact-generated EMP hypothesis was tested by simultaneously tracking of the Moon using AO and HO antennas on 5, 6 May 2014. As it happens, these observations have provided useful insight into unexpected interference from radars on Earth via Moon-bounce. The data collection procedure, methods applied and first results deduced from these observations are presented in the next sections.

2 Methods

2.1 Data Collection

The data collection process was determined by the lunar observation and data-taking capabilities of both the Arecibo (AO) and the Haystack MISA (HO) antenna systems. Due to the location of the HO antenna on the hill, it is entirely steerable to the horizon, and the Moon can be easily tracked from this location. However, AO observing time is constrained to when the Moon is transiting near the zenith at AO as the pointing extends to only about 20° zenith angle. Further, based on observations described in Wen et al. (2007) (for e.g. see Fig. 9c), the maximum sporadic meteoroid flux is seen at dawn for the Arecibo vertical-looking radar system (AO). Therefore, the first quarter phase of Moon is considered as a significant fraction of the visible lunar face is then exposed to the apex-of-Earth's-way and thus to the maximum in sporadic meteoroid flux.

Additionally, during the waxing Moon period (as observed near sunset at AO), the sporadic meteoroid orbits encountered are in solar retrograde motion and thus strike the lunar surface in a head-on manner at maximum relative speed in contrast to the last quarter (waning) phase of the Moon (as observed near sunrise at AO). Figure 1, illustrates the lunar waxing quarter-phase scenario. D represents the Earth Dayside, N for the Nightside of the Earth, and O for the observing location (near zenith at AO) on Earth (at sunset)
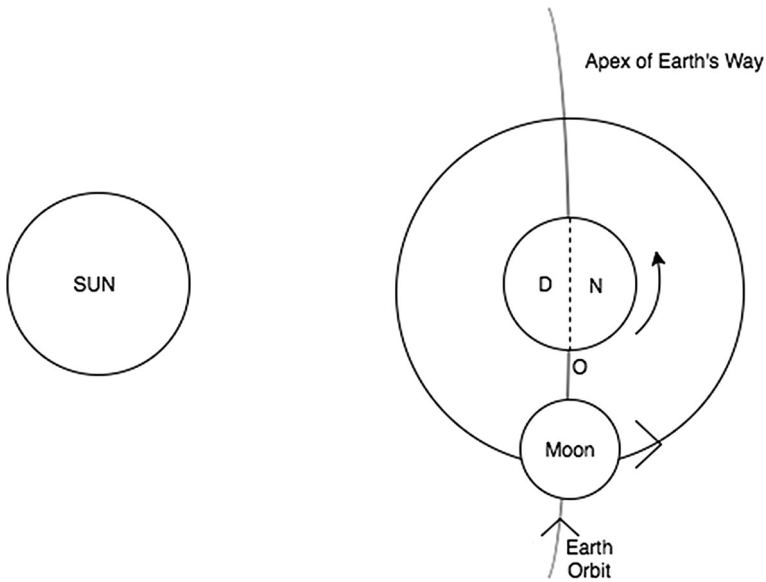
Fig. 1 Illustration of the Sun–Earth–Moon system from above at lunar (M) first quarter when the apex of Earth's way "illuminates" the radar visible surface of the Moon with the apex meteoroid maximum seen 12 h earlier/later with the vertical-looking radar

facing into antapex when most of the AO-visible Moon faces into the apex of Earth's way maximizing the meteoroid flux and detectability from the Earth.

The above criterion for lunar observations at AO is also useful as the lunar radiative temperature is minimum as the dark Moon segment has been dark for 1 week or more and the light-side has been illuminated for 1 week or less thus resulting in minimum noise temperature. Given these considerations and telescope time availability at AO and HO, two consecutive near-sunset observing periods of about 2 h over 20:00 to 23.00 UT hours on 5,6 May 2014 were chosen to observe possible EMPs generated by impacts of the apex-source sporadic meteoroid flux to the Moon as we report here. Note that the limitation on pointing capability at AO reduces the observational time relative to Haystack Observatory.

The observations were divided into active HO radar pulsing mode and in continuous Time-domain radio astronomy (TDRA) mode while receiving at both locations so as to verify the time and frequency coherency between both datasets and the overall tracking. The interleaved HO radar was used in low-power mode for a few minutes every hour to calibrate the monostatic and bistatic lunar results in the manner of Mathews et al. (1988). This monostatic/bistatic pulse-radar mode was used to generate monostatic and bistatic Delay-Doppler radar images, also known as inverse synthetic aperture radar (ISAR; e.g., Chen 2014; Ozdemir 2012) images, of the Moon for a few minutes every hour. This technique is briefly described in Sect. 2.2. As the sub-radar point of the Moon was tracked at both the observatories, TDRA data was collected. A time–frequency analysis technique as described in the second part of the Methods Section was later applied offline to the recorded data in an attempt to detect the hypothesized wide-band, transient signals seen in both datasets at the correct lunar-origin relative delays.

The HO radar system in both active (pulsed radar) and TDRA mode tracked the Moon from just before the Moon entered the AO beam until somewhat after it left the AO beam.

The HO transmitter was operated at a frequency of 440.2 MHz for about 5 min every hour during the observation period. The transmitted signal used was a binary phase-shift code with a net pulse length of 1.69 ms and an interpulse period (IPP) of 40 ms phased such that the full lunar echo fell in between the active transmitter pulsing period when the HO receivers were protected (not receiving). The HO pulse radar transmissions employed right circular polarization and an 845 baud, nested Barker code at 2 µs per baud. This code is generated using two-nested Barker 13 and one Barker 5 code. Additional details about this type of coding are given in Vierinen (2012). In particular, this long code technique is used to achieve a high signal-to-noise ratio and useful range resolution. The transmitted signal was also leaked into the receiver chain for use in later processing stages. The four (two overlapping bands, dual-linear polarization) AO Mock receivers were operated at the system temperature of ~ 50 K—8-bit data was recorded. The single, ~ 300 K receiver at HO was I/Q-sampled on a 25 MHz bandwidth at the expected left-circular receive polarization and stored in 16-bit integer format for later analysis.

The AO 20 MHz bandwidth, dual-circular polarization, 430 MHz Gregorian feed system was used for these observations. It was operated at system temperature ~ 50 K. The data collected at AO was stored in standard Arecibo data format (pdev: http://www.naic.edu/$\sim$phil/pdevall.html) used with the Mock spectrometer receivers in time domain mode. The Mock spectrometers were used to sample orthogonal circular polarizations in two overlapping 10 MHz bands centered at 434 and 438 MHz. The pdev file header contains experiment parameters, Mock spectrometer settings, and the twos-complement in-phase (I) and quadrature (Q) voltages that are stored in 8-bit integer format. The antenna gain at AO is ~ 60 and ~ 42.5 dBi at HO.

Time synchronization of the HO and AO data sets were established using the respective atomic clocks but was also accomplished using the NASA Horizons ephemeris data for the monostatic paths. A separate bistatic ephemeris was generated for these observations (J. D. Giorgini, private communications, 17 Oct 2014). This monostatic ephemeris information is available from NASA's JPL Horizons website (http://ssd.jpl.nasa.gov/). Their web-interface application was used to find the range, the time delay and Doppler shift, and the range–rate of the signal paths to the sub-radar point of the Moon with respect to the observer and transmitter location. The observer locations were set to HO and AO antenna latitude and longitude values and range/delay values to the Moon from both the locations were stored. Additionally, one-way delay values, i.e., the time taken for a signal generated on the lunar surface to reach the observer (both locations), were calculated. These values are used to get the approximate differential time delay within which both the systems in TDRA mode will see the same event. As the Moon and Earth are moving about each other, the one-way delay values change continuously and have to be evaluated for each time stamp of interest in the observation period. Because of the closer distance to the Moon from the AO during the observation period, signals from lunar surface will appear first at AO then at HO. Figure 2, shows the expected delay difference variation during the observation time with values ranging 1.9–2.68 ms on May 5, 2014. Similarly, on the second day of observation, the relative delay varies from 2.4 to 3.1 ms. Therefore, a positive indication of a lunar-originating EMP occurs when an EMP-like signal is observed at both AO and HO within the expected delay difference (see Fig. 2) at a given time of detection.

2.2 Radar Delay-Doppler Lunar-Mapping Technique

Critically, monostatic and bistatic delay-Doppler mapping of the Moon is used to verify our ephemeris and to confirm overall timing. That is, in radar mode, the relative motion
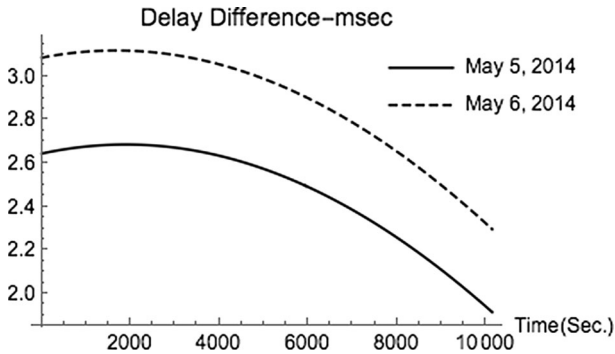
Fig. 2 Delay difference from Ephemeris data. As Moon is close to zenith at AO during the observation period, a lunar-origin signal will arrive first at the AO antenna then at HO. Zero on *x*-axis represents the start time of observation period

between the Moon and the two telescopes is used to image the lunar surface so as to fully calibrate and confirm all timing, Doppler frequency offset, and ephemeris information of the total observing system. As the pulsed HO radar illuminates the Moon, the total monostatic and bistatic time delays serve to calibrate and align pulse information across the full observation window. Further, the reflected signals at delays beyond the first return (from the monostatic/bistatic subradar points) correspond, for each range gate, to all of the points on the circle centered on the subradar point at that delay. Additionally, when the target spins about its axis, all of the scattering features on a given Doppler shift "circle" either move towards or away from the receiver with respect to the Doppler shift at the subradar point. Hence, Doppler and delay information of the reflected pulse can be used to map or image the radar surface of the target [see Fig. 1, Hagfors and Kofman (1991)]. As the degree of dispersion (F = TB, T = target delay depth, B = target Doppler half-width at observation frequency) of the Moon at 440.2 MHz is F ~ 0.127, it is an under spread target and thus the standard Delay-Doppler mapping technique, as described in Harmon (2002), was chosen for imaging. The radar delay depth of the Moon is ~ 11.57 ms, and the half Doppler width of the Moon at 440.2 MHz is ~ 11 Hz. The total Earth-Moon delay time is ~ 2.6 s and an IPP of 40 ms is phased such that the full lunar echo arrived between radar pulses. The lunar echo was sampled at 10 MHz at AO and 25 MHz at HO.

In the signal-processing path—outlined in Fig. 3—the received raw complex (I/Q) voltage samples are stored for later offline processing that includes a preprocessing range and phase alignment stage, decoding, azimuth FFT, and finally incoherent averaging to generate the desired Delay-Doppler image. In the first pre-processing stage, as lunar range changes over each IPP, returns from each pulse return must be aligned (based on the ephemeris) such that beginning of each pulse is at the same data array row index (note that samples are available every 0.1 µs or faster).

Further, the Doppler center of each pulse is slightly different which also causes blurring unless compensated via continuous phase adjustment via mixing each signal to a common zero Doppler shift. Both range and phase adjustments are based on the ephemeris infor-mation. Various motion compensation techniques enabling the mapping or imaging of moving targets are described in the Inverse Synthetic Aperture Radar Technology (ISAR) literature (e.g., Chen and Andrews 1980).

To clarify the preprocessing steps, both the range alignment and phase adjustment were achieved using ephemeris delay and ephemeris Doppler values of the respective
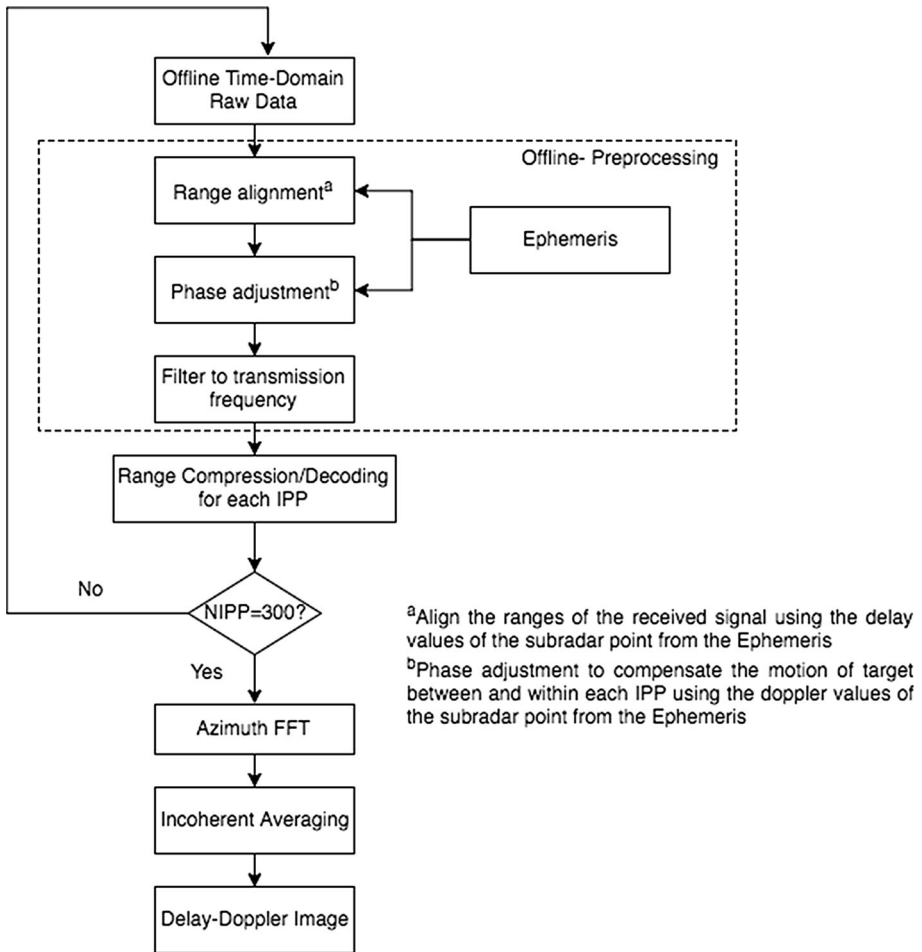
Fig. 3 Lunar delay-Doppler imaging signal processing path

monostatic (HO) and bistatic (HO/AO) subradar points of the target. Aligning the ranges of each IPP using the delay values of the sub-radar point performs the coarse range alignment. The phase adjustment to remove the phase changes because of the motion, i.e. range–rate, is performed using Eqs. (1–3) below.

$$\phi'_{l1} = 1 \tag{1}$$

$$\phi'_{lj} = \phi'_{lj-1}e^{-i2\pi f_d\left(t_{lj}-t_{lj-1}\right)} \quad j = 2,3,4,\dots N \quad i = l \tag{2}$$

$$\phi'_{ij} = \phi'_{lj}e^{-i2\pi f_d\left(t_{ij}-t_{lj}\right)} \quad i = 2,3,4,\dots M \quad j = 1,2,\dots N \tag{3}$$

where i, j represent the range and IPP or profile number respectively. M, N is the total number of ranges and profiles to be processed, respectively. The range of the subradar point in each pulse is represented by l. The phase of the subradar point of the first pulse is considered as the reference point in Eq. (1). The phase changes of the subradar point in the

adjacent pulses (ϕ_{lj}) w.r.t to the subradar point in the reference pulse are then estimated using the instantaneous Doppler values (f_d) from the Ephemeris data and the progressive phase adjustment described by Eq. (2). Further, phase change of the rest of the target scatter points(delay-Doppler "pixels") located in the remaining range bins w.r.t to the sub-radar point for each IPP or pulse are adjusted as described by Eq. (3). The estimated phase differences (ϕ'_{ij}) are then multiplied with initial coarse aligned complex range and profile values. This procedure, which results in a common Doppler offset due to range-rate removal, is analogous to the second scheme for motion compensation described in Chen and Andrews (1980) and the modified version of the offline focus methodology described in Vierinen and Lehtinen (2009).

In the next step, the range- and phase-aligned pulse data are filtered to a center (transmitter) frequency of 440.2 MHz at a 1 MHz bandwidth and decoded by effectively cross-correlating the processed signal with the measured transmitted Barker code (matched filtering) as described in Sect. 2. The matched filtering process corresponds to the measured transmitted code at zero frequency shift. For these observations, the maximum range rate is 90 m/s corresponding to a Doppler shift of 265 Hz. This decoding technique, shown as the range compression stage in Fig. 3, is repeated for all of the consecutive pulses (in 300 IPP groups in our example) with the results stored in appropriate arrays. In Fig. 4, we give example decoded time series of the lunar echo in the monostatic and bistatic cases. The power drop-off versus delay towards the limb of the Moon is similar to the observations discussed in Thompson and Dyce (1966).

Once the entire decoded dataset is aligned and filtered, the third processing stage involves 2D Fourier transforming the entire voltage sequence at each range gate yielding an estimate of the Doppler power spectrum at each range from the leading edge to the lunar limb. This step is also known as azimuth FFT compression as indicated in Fig. 3. A typical bistatic power spectrum—in this case at 1.2 ms delay beyond the leading edge—is shown in Fig. 5. Lastly, the consecutive 300-IPP power spectrum values in all range gates are incoherently averaged to produce the desired higher-SNR Delay-Doppler images shown in Fig. 6.

To emphasize the issues surrounding the proper time alignment within two datasets, for each of the 300 inter pulse period samples transmitted at six regular intervals during the observation period, absolute mean error and the standard deviation of the difference between the observationally-estimated sub-radar point delay values and the delay values from the ephemeris are calculated as shown in Table 1. The estimated sub-radar point delay is calculated by detecting the range that has maximum peak power within each pulse
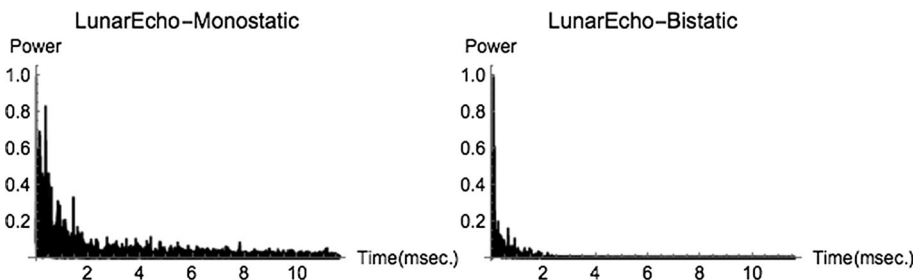
Fig. 4 Example monostatic (*left panel*) and bistatic (*right panel*) lunar echoes. The full lunar delay depth is ∼11.6 ms is shown in both cases. Since the AO beam is narrow (∼1/6th degree) the bistatic echo beyond ∼4 ms is just the net thermal noise

Fig. 5 An example HO–AO lunar power spectrum return at lunar delay depth of 1.2 ms
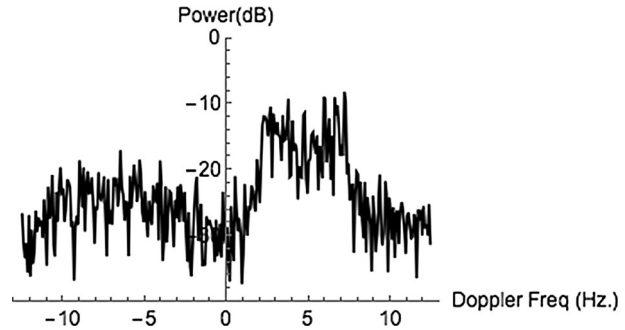
from the properly decoded voltage values. Then, respective delay of this subradar point to the transmission time is calculated based on the start time of the respective (recorded) transmitted pulse. From Table 1, it can be seen that maximum error in timing difference is 113 and 104.8 μs for the HO and AO datasets respectively.

Further, as the one way delay-difference between both the observatories—per Fig. 2 and as summarized in the last column of Table 1 for the respective intervals—is in the range of milliseconds, the percentage error corresponding to the measured time difference to the one-way delay difference is less than 5 % during the whole period of observation, lending confidence to the lunar EMP observations conducted jointly at both HO and AO. Henceforth, this mapping technique serves to determine and verify the timing at both the observatories to enable the EMP search described below.

2.3 Passive EMP Time–Frequency Signal Detection Technique

The time–frequency characteristics of the data from the TDRA mode are studied by applying the Short-Time Fourier Transform (STFT; e.g.,Wen et al. 2005) on the wideband, time series data. The STFT analysis approach projects the data into spectral power density versus frequency over short time intervals. The search for EMP characteristics within these results then requires a separate search algorithm outlined next.

In particular, as the hypothesized EMP event time scale ($\sim$ 1–50 μs) is smaller, relative to the observation period (h), far too many spectrograms will be generated for a manual search for wideband signals to be practical. Therefore, to increase the efficiency and decrease effective processing time, an automatic algorithm, outlined in Fig. 7, was implemented to search the STFT results for events exhibiting EMP-like characteristics (short time duration and wideband) in the higher-SNR, lower-interference AO dataset. Possible events were then crosschecked in the HO data at the expected delay window, centered at $\sim$ 2.5 ms (see Fig. 2), for an event delay consistent with an EMP originating on the lunar surface.

The first step in implementing the Fig. 7 scheme is to choose the optimal time-window size, generate the STFT spectra, and search within it for an appropriate signal(s) above the noise level. The window size must be carefully balanced to yield sufficient time and frequency resolution because of the fixed resolution that the STFT technique provides. A wide time window gives better frequency resolution but poor time resolution, and a narrow window gives better time and poorer frequency resolutions (Chap. 9, Son et al. 2001). As the EMP signal to be detected is hypothesized to be less than 100 microseconds in duration and wideband in nature, we chose the "block" time window to be 1 ms or 10,000 samples
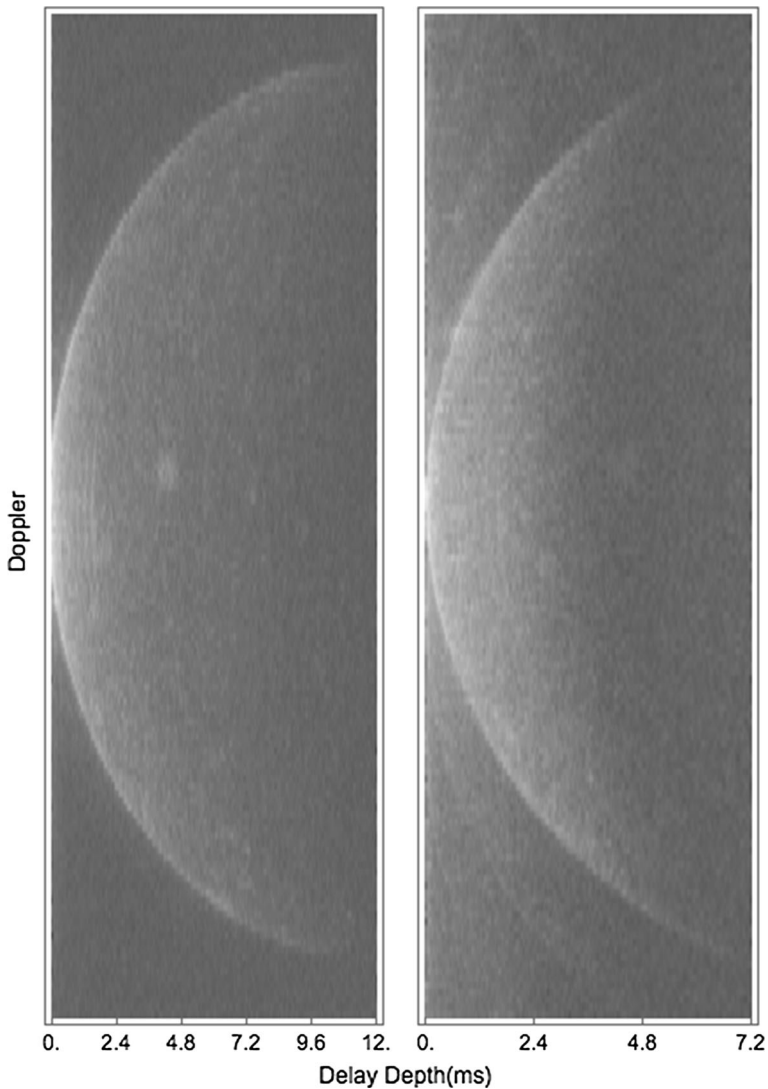
Fig. 6 Delay Doppler HO–HO monostatic image to the *left* and HO–AO bistatic image to the right at the transmission unixtime 1,399,322,650 s. The number of IPP's used coherently (ISAR imaging) is 300 i.e., a coherent integration time of 12 s. *Rows* represent the Doppler axis and *Columns* represent the Delay axis with resolution of 150 m along delay and 21 km along the Doppler axis. The lunar full delay depth of ~ 11.6 ms is seen in the monostatic image and of ~ 5 ms in bistatic image due to the narrow beam width of Arecibo Antenna

within which 117 STFTs are performed by partitioning the time-window into short-time subsets with an offset of 8.5 µs (rectangular window). These parameters yield a time resolution of 8.5 µs and frequency resolution of 39 kHz (256 Fourier points) for AO dataset that was sampled at 10 MHz.

   In the next step, the individual spectral magnitudes at each time increment are averaged and squared creating a short-time power series of the length of 117. This procedure

Table 1 Mean and standard deviation of the timing error in both datasets at regular intervals during the observation period

First-transmit pulse time (Unix Time)	Absolute mean error in AO dataset (μs)	Standard deviation of the error in AO dataset (μs)	Absolute mean error in HO dataset (μs)	Standard deviation of the error in HO dataset (μs)	One-way delay difference between HO and AO (ms)
1,399,322,650	80.6	26.8	102.4	24.7	2.68
1,399,326,748	78.1	35.7	113	16.8	2.48
1,399,329,620	77.2	19.0	98.5	18.8	2.1
1,399,412,220	92.9	25.7	105.5	19.1	3.1
1,399,415,810	104.8	20.0	82.7	19.4	2.9
1,399,417,510	89.7	33.6	99.6	25.6	2.7

By "timing error" we mean the difference between the radar-determined delay to the lunar subradar point and the delay given by the ephemeris. The approximate RMS error in the observed total subradar point delay is 133.5 μs
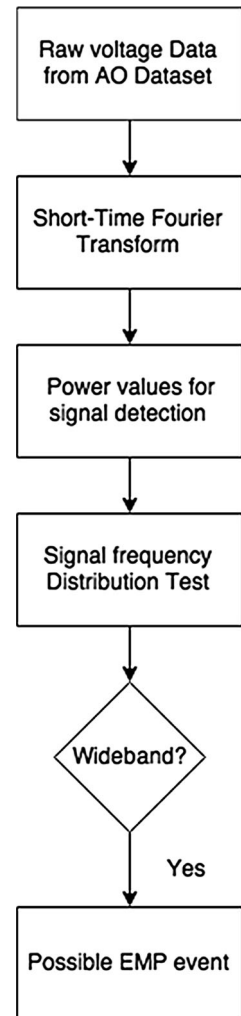
suppresses noise, and the distinct time–frequency features expected for EMPs are detected. Using a threshold set by the observed off-Moon noise levels mentioned in Sect. 2.

If a feature above the threshold is detected, the absolute spectral values at all the frequencies at that particular time within the 1 ms window are subject to a statistical distribution test to check if the feature is of wideband nature. This normal distribution test is done via the common method of statistical hypothesis testing (Walpole et al. 1993).To be specific, this test performs a goodness-of-fit hypothesis test with null hypothesis that data was drawn from population with a specified distribution, e.g. a normal distribution, and an alternative hypothesis that it is not. The Mathematica algorithm used automatically chooses various statistical distribution test functions including the Anderson–Darling test and the Pearson's Chi squared test to determine the P value. If the P value, i.e. the probability that distribution is normal crosses the fixed threshold (95 % confidence interval), it is marked as the possible short time (transient)-wideband event as all of the spectral values clusters about the same mean.

3 Results and Discussion

The results reported in this section are obtained by processing and analyzing the joint AO/HO 4-h data sets collected on 5 May 2014 from 20:11 to 23:00 Universal Time (UT) and on 6 May 2014 from 21:00 to 23:50 UT. The Moon "rose" into the AO beam at about 20:20 UT on the first day and at about 21:10 UT on the second day. The active radar mode was operated for approximately 5 min intervals at 20:45, 21:45, 22:40 UT on 5 May 2014 and at 21:35, 22:35, and 23:00 on 6 May 2014. Outside of these intervals, both systems were operated in TDRA mode until the Moon exited the AO beam at the end of observations around 22:45 UT and 23:45 UT on the first and second days, respectively.

Fig. 7 Passive EMP time–
frequency signal detection
processing flowchart

```
┌─────────────────────┐
│  Raw voltage Data   │
│   from AO Dataset   │
└─────────────────────┘
           │
           ▼
┌─────────────────────┐
│ Short-Time Fourier  │
│     Transform       │
└─────────────────────┘
           │
           ▼
┌─────────────────────┐
│   Power values for  │
│   signal detection  │
└─────────────────────┘
           │
           ▼
┌─────────────────────┐
│  Signal frequency   │
│  Distribution Test  │
└─────────────────────┘
           │
           ▼
        ◇ Wideband? ◇
           │
           │ Yes
           ▼
┌─────────────────────┐
│  Possible EMP event │
└─────────────────────┘
```

3.1 Monostatic and Bistatic Radar Lunar Images

As mentioned above a series of brief radar transmission sessions were used to calibrate the monostatic and bistatic lunar observing paths, thus confirming the ephemeris, system stability, time stamping, etc. in both data sets. Figure 6 shows the proof of our success in this regard in the example monostatic and bistatic Delay-Doppler lunar images generated for case by processing the active radar data collected in the 20:45 UT interval on 5 May 2014. As discussed above, we used a 2 μs baud binary (Barker) coded transmitted pulse yielding a nominal 300 m range resolution. However, our effective range resolution is given by

$$\Delta R = c/2B \qquad (4)$$

where B is the fully-sampled bandwidth of the receiver and c is the speed of light. The AO receivers have a bandwidth of 10 MHz and HO receiver has the bandwidth of 25 MHz.

Therefore the respective range resolution values are in principle 15 m and 6 m. However, we coherently average the received voltage to a final delay/range resolution of 150 m. The Doppler Resolution is given by the pulse repetition frequency (PRF) and the number of integration pulses (N) used in the Fourier transform as in Eq. (5),

$$\Delta D = PRF/N \tag{5}$$

In this case, the PRF (= 1/IPP) is 25 Hz and N = 300 pulses were yielding a spectral resolution of 0.083 Hz. The Doppler resolution that is required to observe with a 1 km resolution, given the 11 Hz Doppler half-bandwidth of the Moon (radius of $\sim$1738 km), is 0.0031 Hz/km. Therefore the 0.083 Hz frequency resolution corresponds to a lunar-limb spatial resolution of $\sim$26 km. Increasing N can improve the resolution, however this requires more computational time and lowers the SNR as fewer spectra are incoherently added given the short radar observing intervals. Moreover, because of the narrow beam width of AO antenna, $\sim$0.2° as compared to the apparent Moon's angular resolution of 0.5°, the resultant bistatic image shows only $\sim$1/3 part of the Moon centered at the bistatic subradar point whereas the HO antenna beamwidth is $\sim$1.2° and shows the full visible side of the lunar surface. Having successfully generated these monostatic and bistatic images demonstrates full calibration of both the datasets in time and frequency as, without proper alignment in time and frequency, proper decoding would fail and the Delay-Doppler mapping would not succeed.

3.2 Search for EMPs

While the lunar radar images serve to confirm net system calibration, the search for wide-band impulsive signals (EMPs) generated on the Moon presents different signal processing challenges. As described previously, a signal detection procedure based on Short-Time Fourier Transforms (STFT) was used to search for EMPs. However, we discovered a wide variety of terrestrial signals reflected from the Moon along with severe local interference at HO that complicated the search.

In particular, terrestrial radar signals reflected off of the Moon, i.e., terrestrial-origin Moon-bounce (TOMB) signals, dominated our detection scheme as shown in Fig. 8. Various distinctive short- and long-duration frequency-dispersive (CHIRP; compressed high-intensity radar pulse) signals with different polarization characteristics were observed with—appropriately—a few such events observed at both locations with the appropriate two-way delay thus further confirming our system calibration. Most of these events have the chirp characteristics of military radars and were observed only at AO. The stronger events display the characteristic limb-scattering features for a Moon-bounce signal. Example events are given in Figs. 8 and 9. These dispersive TOMB signals decay in time due to progressive limb scattering from the Moon's surface as further demonstrated in Fig. 10. Moreover, most of the wider dispersive signals have a linear chirp width of 5–10 MHz and pulse duration of $\sim$4–8 ms thus characterizing these signals to be from one of the ground-radars operating between 420 and 450 MHz used for space object tracking and cataloguing as described in NTIA (2014), ITU (2000). Further, the time difference of the common HO/AO event i.e. 2.56 ms closely match with the delay difference value calculated from the ephemeris at that particular time i.e. 2.59 ms confirming that they are terrestrial origin signals bouncing off the Moon's surface. Lunar reflections of terrestrial radio leakage reflected off the Moon were also observed at AO previously in 150–500 MHz range as discussed in Sullivan III and Knowles (1985). They also concluded
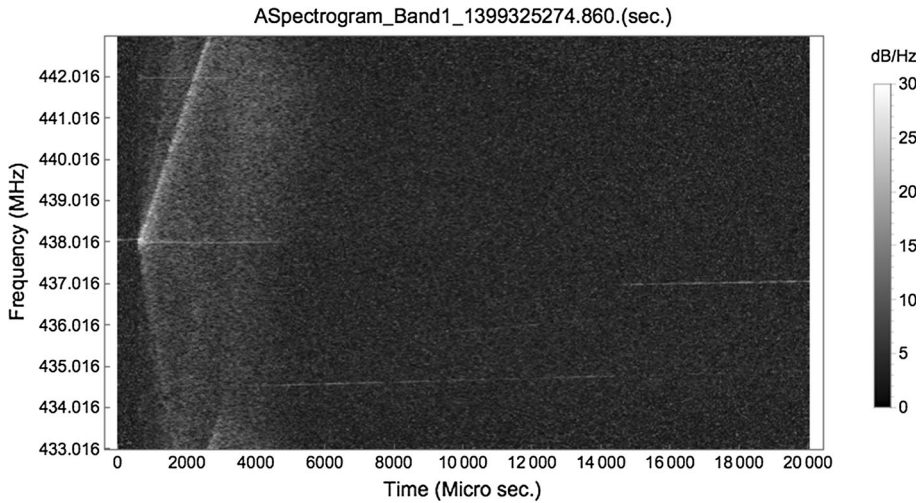
Fig. 8 Spectrogram of terrestrial origin-Moon bounce (TOMB) signal from AO band1 observations is shown starting at ∼500μs. This is likely a frequency-chirped radar pulse that saturated the 8-bit sampling settings causing the extra features
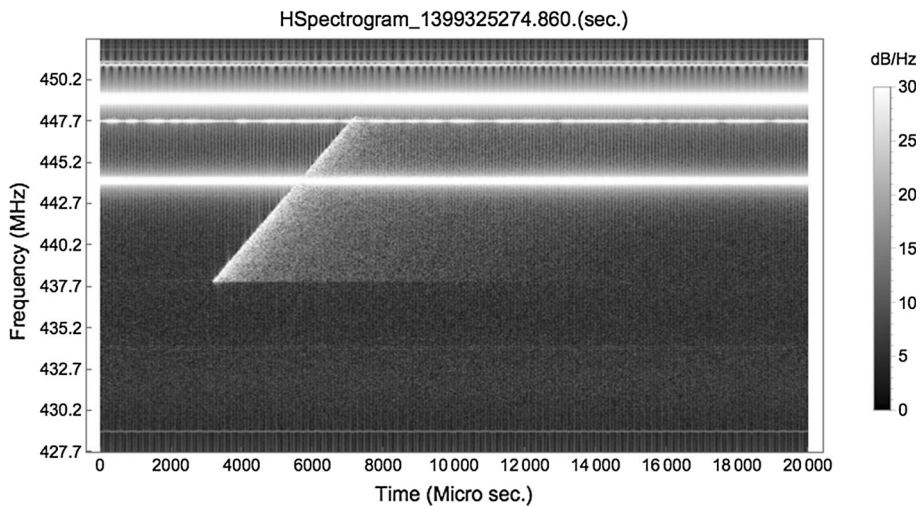
Fig. 9 Spectrogram of a terrestrial origin-Moon bounce (TOMB) signal in HO observations. *Note* the strong local interference and lunar-limb scattering of the TOMB signal in these results and the delay difference with the same signal observed at AO as shown in Fig. 8

from their observations that main contributors for what we term TOMB signals are military radars and television transmitters. Note, that a TOMB signal with EMP-like signal characteristics if present will show signs of lunar limb scattering thus immediately eliminating it as an EMP event caused by the meteoroid impact on lunar surface.

In addition to many TOMB signals, the algorithm detected a few (i.e., 5–10) wideband events on each day. The duration of these events is few 10's to 100 microseconds with signal strength varying in the range of 40–50 dB compared to the background noise. They
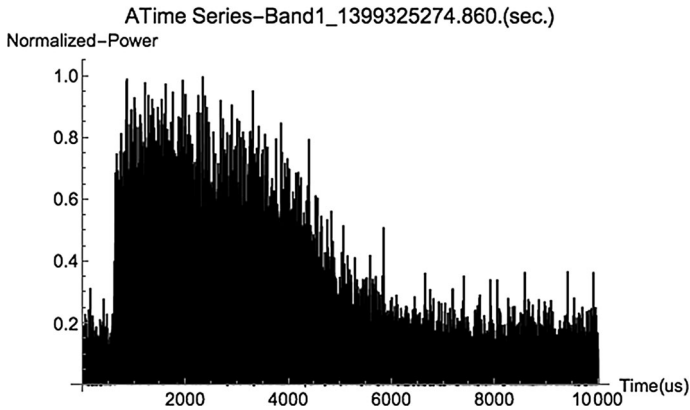
Fig. 10 Time series plot of the terrestrial origin-Moon bounce (TOMB) signal shown in Fig. 8. *Note* the decay in the power values versus the delay

are detected in both polarizations and both the bands in the AO data when the Moon was being tracked. One such example of a possible EMP event is discussed and shown in Figs. 11 and 12. These AO band0 and band1 spectrograms, respectively, show both TOMB and a EMP-candidate wideband event during the same time frame. In particular, we observe three prominent signals. Two of them are the strong and separate TOMB signals with beginning time at approximately around 1800 μs and starting frequency at 437 and 442 MHz respectively. The third event is a wideband transient signal starting at 11,600 μs that has a signal duration of ∼42 μs. The time series of this signal is shown in Fig. 13. Among these three signals, the first TOMB signal is seen in HO data at the respective delay difference i.e. starting at ∼4000 μs that has low signal to noise ratio value and similar time–frequency characteristics (see Fig. 14). Further, from Fig. 2, the expected delay
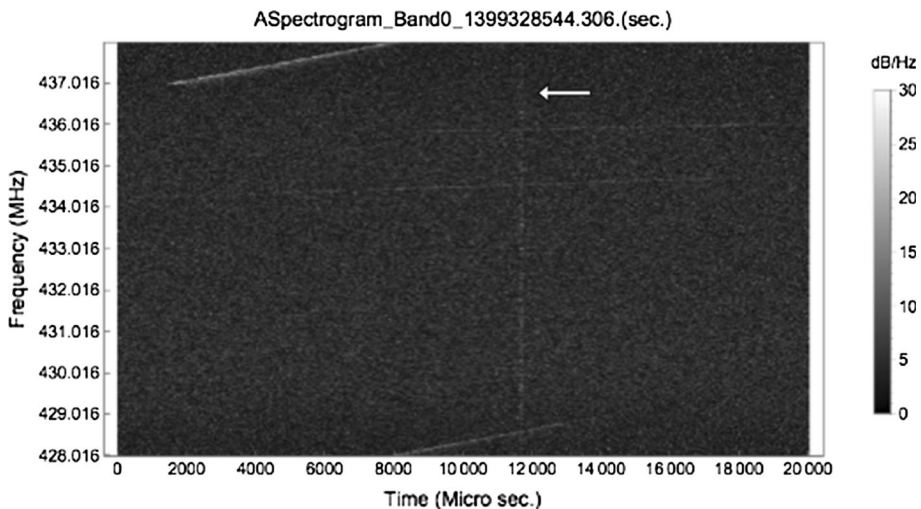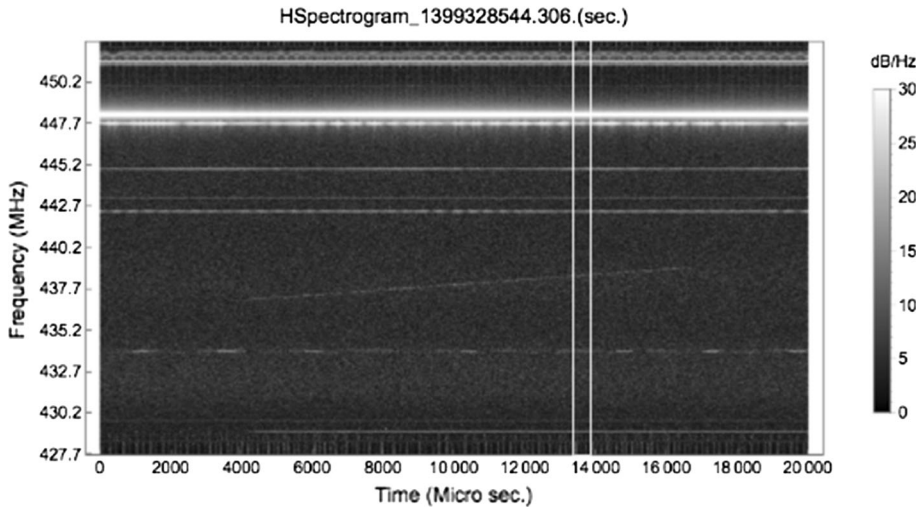

Fig. 11 Spectrogram from the AO Band0 observations starting at unixtime 1,399,328,544.306 s. *Note* the spectrogram of a possible EMP event at ∼11,600 μs and one TOMB signal starting at ∼1800 μs at ∼437 MHz within the time window of 20 ms
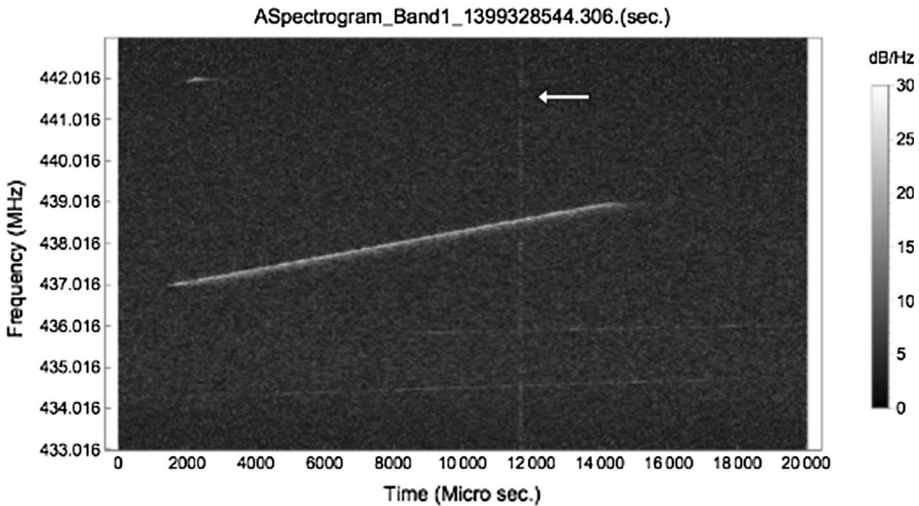
Fig. 12 Spectrogram from the AO Band1 observations starting at unixtime 1,399,328,544.306 s. *Note* the spectrogram of possible EMP event at ∼11,600 μs and two TOMB signals starting at ∼1800 μs at ∼437 MHz and ∼442 MHz within the time window of 20 ms
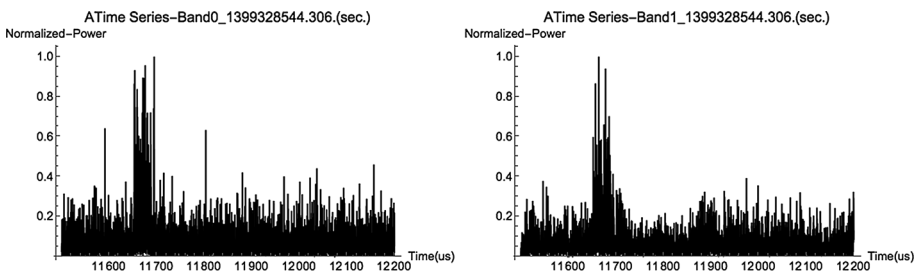

Fig. 13 Time series plot of the possible EMP event shown in Figs. 11 and 12. To the left is the time series plot from AO Band0 and to the right is from Band1 observations. The time duration of the event is ∼42 μs

difference is nearly 2.2 ms. However, the transient wideband signal and the second TOMB signal were not observed at a respective lunar-origin delay in HO data as seen in Fig. 14. The delay window expected for the Figs. 11 and 12 EMP-candidate is within the box shown in Fig. 14. The possible reason for no HO detection of EMP-candidate event could be the lower sensitivity of HO antenna. Given the SNR difference in the common TOMB event at this time, the candidate-EMP would be only marginally observable at HO. This is due to both the intrinsic sensitivity difference and to the reduction in sensitivity due to processing through the strong interference levels observed at the higher frequencies from the amateur radio repeater sources.

Further, at short time scales in HO data (see Fig. 15) the power-line interference is identified as caused by arcing across bad insulators in the transformer yard next to the HO radar. Other possible EMP sources can be electrostatic discharge due to the natural sources like lightning (Le Vine 1980). Such local sources, if present, will illuminate only the nearby antenna feed and will only be observed at that location. While signal processing can mitigate the effects of these local interference sources, it is impossible to fully evaluate the

Fig. 14 Spectrogram from the HO observations starting at unixtime 1,399,328,544.306 s. A linear chirp TOMB signal similar to the observed signal in AO data as shown in Fig. 12 starting at ∼4000 μs is observed. The *white box* outlines the window within which the Figs. 11 and 12 candidate-EMP should appear at Haystack
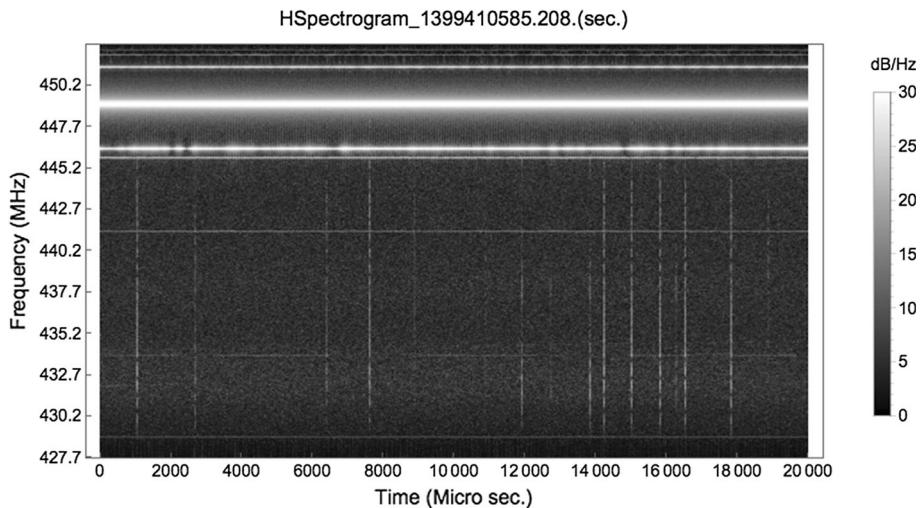
Fig. 15 Spectrogram from the HO observations starting at unixtime-1,399,410,585.208 s that shows the local transient power-line interference signal along the time window and amateur radio repeater interference signal at frequencies greater than 445 MHz

success of this approach. It is far better to eliminate the interference for future observations. Secondly, based on the ITU standards described in NTIA (2014), ground-based radars operating in this frequency range (420–450 MHz) should not be transmitting circularly polarized, microsecond duration wideband signals. Thus while the candidate-EMP signals were not observed at the respective lunar delay difference at both the locations, the dual-polarization and short-duration with rapid onset features of the candidate-EMPs allow

us to tentatively conclude that these signals originated due to meteoroid impacts on the lunar surface.

4 Conclusion

In this paper, we hypothesized that ElectroMagnetic Pulse (EMP) signals of transient and wide-band nature are generated when gram or larger size meteoroids impact the lunar surface. Based on this hypothesis, we used the HO and AO radar systems operating near 440 MHz frequency in both active radar and TDRA (Time-Domain Radio Astronomy) modes in two sets of observations to search for EMPs and to cross-calibrate the systems while simultaneously tracking the Moon. Delay-Doppler radar imaging of the Moon was used to confirm overall calibration and synchronization of the two systems while Time–frequency signal detection methods were applied to search for lunar meteoroid impact generated EMPs. Even though the hypothesized EMP events were not conclusively detected, we have established that the results (Figs. 8, 9) validate the observational setup and observations as both of the TDRA receive systems see the same common terrestrial origin Moon bounce (TOMB) events. Further, we report the AO detection of candidate-EMP events that, while not observed at HO, should not have been detected given the sensitivity difference in the two systems and the high level of interference at HO during these observing periods.

To increase the chances of valid EMP detection, future observations have to be conducted when the power-line arcing in the transform yard at HO has been eliminated. Additionally, amateur radio repeater interference removal techniques have to be developed to clean and process the data collected at the HO. The upper-frequency can also be limited to 445 MHz to avoid the interference signals although strong, out-of-band signals would remain an issue. Alternatively, the Arecibo L-band ALFA array covers the "protected" cold-hydrogen radio astronomy band (57 MHz bandwidth from 1.37 to 1.427 GHz) and offers an alternative EMP search mechanism that uses the cluster of seven dual polarization feeds that together largely illuminate the Moon. These observations were proposed and conducted on 02–14–2016 at AO with data reduction ongoing. Further, possible simultaneous optical telescope lunar observations during the radio observations may, with considerable luck, detect an EMP associated with a bright lunar meteoroid impact optical flash.

References

C.-C. Chen, H.C. Andrews, Target-motion-induced radar imaging, in *IEEE Transactions on Aerospace and Electronic Systems*, pp. 2–14 (1980)

V.C. Chen, *Inverse Synthetic Aperture Radar Imaging Principles, Algorithms and Applications* (SciTech Publishing, an imprint of the IET, Edison, NJ, 2014)

S. Close, P. Colestock, L. Cox, M. Kelley, N. Lee, Electromagnetic pulses generated by meteoroid impacts on spacecraft. J. Geophys. Res.: Space Phys. **115**, A12328 (2010)

S. Close, I. Linscott, N. Lee, T. Johnson, D. Strauss, A. Goel, et al., Detection of electromagnetic pulses produced by hypervelocity micro particle impact plasmas. *Phys. Plasmas (1994-present)* **20**, 092102 (2013)

A. Collette, K. Drake, A. Mocker, Z. Sternovsky, T. Munsat, M. Horanyi, Time-resolved temperature measurements in hypervelocity dust impact. Planet. Space Sci. **89**, 58–62 (2013)

L. Foschini, Electromagnetic interference from plasmas generated in meteoroids impacts. EPL (Europhys. Lett.) **43**, 226 (1998)

J.F. Friichtenicht, J.C. Slattery, Ionization associated with hypervelocity impact, TND2091 (1963). https://ntrs.nasa.gov/archive/nasa/casi.ntrs.nasa.gov/19630010729.pdf

T. Hagfors, W. Kofman, Mapping of overspread targets in radar astronomy. Radio Sci. **26**, 403–416 (1991)

J.K. Harmon, Planetary delay-Doppler radar and the long-code method. IEEE Trans. Geosci. Remote Sens. **40**, 1904–1916 (2002)

ITU, Characteristics of and protection criteria for radars operating in the radiolocation service in the frequency range 420–450 MHz, M.1462, (2000). https://www.itu.int/dms_pubrec/itu-r/rec/m/R-REC-M.1462-0-200005-I!!PDF-E.pdf

T. Johnson, I. Linscott, S. Close, D. Strauss, N. Lee, R. Adamo, et al., Detection and analysis of RF data from hypervelocity impacts, in *Proceedings of 3rd AIAA Atmosphere Space Environment Conference*, (2011), pp. 1–9

M.A.M. Larbi, A. Daassou, D. Baratoux, S. Bouley, Z. Benkhaldoun, M. Lazrek et al., First lunar flashes observed from Morocco (ILIAD Network): implications for Lunar seismology. Earth Moon Planet **115**, 1–21 (2015)

D.M. Le Vine, Sources of the strongest RF radiation from lightning. J. Geophys. Res.: Oceans **85**, 4091–4095 (1980)

N. Lee, S. Close, D. Lauben, I. Linscott, A. Goel, T. Johnson et al., Measurements of freely-expanding plasma from hypervelocity impacts. Int. J. Impact Eng. **44**, 40–49 (2012)

J. Madiedo, J. Trigo-Rodriguez, Historical records of delta-arietids superfireballs over Spain, in *Lunar and Planetary Science Conference*, p. 1368 (2011)

J.M. Madiedo, J.L. Ortiz, N. Morales, J. Cabrera-Caño, A large lunar impact blast on 2013 September 11. Month. Notices R. Astron. Soc., p. stu083 (2014)

K. Maki, E. Soma, T. Takano, A. Fujiwara, A. Yamori, Dependence of microwave emissions from hypervelocity impacts on the target material. J. Appl. Phys. **97**, 104911 (2005)

K. Maki, T. Takano, A. Fujiwara, A. Yamori, Radio-wave emission due to hypervelocity impacts in relation to optical observation and projectile speed. Adv. Space Res. **34**, 1085–1089 (2004)

H. Martinides, Extraterrestrial Noise in the (Noise from the Moon) UHF Region (300–3000 Mc) (1965). http://ntrs.nasa.gov/archive/nasa/casi.ntrs.nasa.gov/19650026836.pdf

J. Mathews, J. Breakall, M. Sulzer, The Moon as a calibration target of convenience for VHF-UHF radar systems. Radio Sci. **23**, 1–12 (1988)

N. McBride, J. McDonnell, Meteoroid impacts on spacecraft: sporadics, streams, and the 1999 Leonids. Planet. Space Sci. **47**, 1005–1013 (1999)

I. Nemtchinov, V. Shuvalov, N. Artem'eva, B. Ivanov, I. Kosarev, I. Trubetskaya, Light flashes caused by meteoroid impacts on the lunar surface. Sol. Syst. Res. **32**, 99 (1998)

NTIA, 420–450 MHz, 0420.00-0450.00_01MAR14, (2014) https://www.ntia.doc.gov/files/ntia/publications/compendium/0420.00-0450.00_01MAR14.pdf

J. Ortiz, F. Aceituno, J. Quesada, J. Aceituno, M. Fernández, P. Santos-Sanz et al., Detection of sporadic impact flashes on the Moon: implications for the luminous efficiency of hypervelocity impacts and derived terrestrial impact rates. Icarus **184**, 319–326 (2006)

C. Ozdemir, *Inverse synthetic aperture radar imaging with MATLAB algorithms*, vol. 210 (Wiley, New Jersey, 2012)

P.R. Ratcliff, M.J. Burchell, M.J. Cole, T.W. Murphy, F. Alladfadi, Experimental measurements of hypervelocity impact plasma yield and energetics. Int. J. Impact Eng **20**, 663–674 (1997)

J.J. Rembold, E.V. Ryan, Characterization and analysis of near-earth objects via lunar impact observations. Planet. Space Sci. **117**, 119–126 (2015)

J.S. Son, G. Thomas, B. Flores, *Range-Doppler Radar Imaging and Motion Compensation* (Artech House Inc., London, 2001)

R. Suggs, D. Moser, W. Cooke, R. Suggs, The flux of kilogram-sized meteoroids from lunar impact monitoring. Icarus **238**, 23–36 (2014)

R.M. Suggs, W.J. Cooke, R.J. Suggs, W.R. Swift, N. Hollon, The NASA lunar impact monitoring program. Earth Moon Planet **102**, 293–298 (2008)

W.T. Sullivan III, S.H. Knowles, Lunar reflections of terrestrial radio leakage, in *The Search for Extraterrestrial Life: Recent Developments*, (Springer, 1985), pp. 327–334

T. Thompson, R. Dyce, Mapping of lunar radar reflectivity at 70 cm. J. Geophys. Res. **71**, 4843–4853 (1966)

J. Vierinen, *On Statistical Theory of Radar Measurements* (Aalto University, Espoo, 2012)

J. Vierinen, M.S. Lehtinen, 32-cm wavelength radar mapping of the Moon, in *Proceedings of the 6th European Radar Conference* (2009)

R.E. Walpole, R.H. Myers, S.L. Myers, K. Ye, *Probability and Statistics for Engineers and Scientists*, vol. 5 (Macmillan, New York, 1993)

C.-H. Wen, S. Briczinski, D. Livneh, J. Doherty, J. Mathews, Pulse-level interference and meteor processing of Arecibo ISR data. J. Atmos. Solar Terr. Phys. **69**, 973–980 (2007)

C.-H. Wen, J. Doherty, J. Mathews, Adaptive filtering for the separation of incoherent scatter and meteor signals for Arecibo observation data. J. Atmos. Solar Terr. Phys. **67**, 1190–1195 (2005)